Supporting Information

Johnson et al. 10.1073/pnas.1305530110

SI Text

Sample Collection

GEC01 and GTF01 cores were drilled in the Northern Cape Province of South Africa as a part of a second phase of the South African Agouron drilling project. These two cores capture the Koegas Subgroup of the Ghaap Group and a portion of the overlying Postmasburg Group (Fig. S1). The Koegas Subgroup overlies the Asbestos Hills Subgroup, comprised of the Kuruman and Griquatown Formations. The upper Kuruman formation has ash beds dated by U-Pb sensitive high-resolution ion microprobe (SHRIMP) on zircons to 2,460 ± 5 Ma (1) and the Griquatown Formation has zircons dated by U-Pb SHRIMP to 2,431 ± 31 Ma from published conference proceedings (2, 3). Overlying the Koegas Subgroup is the Makganyene Formation [a glaciogenic unit deposited on top of a substantial regional unconformity (4–6)] and the Ongeluk Formation, which has been dated by whole-rock Pb-Pb isochron to 2,238 ± 90 Ma (7, 8) and refined in a later study to 2,222 ± 12 Ma (9). Zircons from an ash bed in the Rooinekke Formation of the Koegas Subgroup were dated by SHRIMP U-Pb to 2,415 ± 6 Ma in a technical report (5, 10), which currently constitutes the best age constraint for the Koegas Subgroup (5, 6, 11–13). Cores were slabbed and logged, and half was sent to the California Institute of Technology with the other half archived at the Council for Geoscience in South Africa. Details of the sedimentary geology and bulk geochemistry can be found in Schröder et al. (5). Subsamples for petrographic and geochemical analysis were collected from the cores using nonmagnetic blades and bit on a trim saw and drill press, respectively.

Sample Preparation and Bulk Element Geochemistry

A preliminary dataset for the major, minor, and trace element geochemistry was acquired at the University of Johannesburg analytical facility (5). Wavelength-dispersive X-ray fluorescence analyses (XRF) were used on the lithium borate ($Li_2B_4O_7$-$LiBO_2$) fused glass beads on a Philips Magix Pro Spectrometer. Elemental composition was determined with precision better than 0.5% and accuracy better than ±5% for most elements except iron, which was better than ±10%. A second set of core subsamples was analyzed for bulk chemistry in the Activation Laboratories, Ancaster, Ontario. Chips of core (0.5 g each) were pulverized and digested in aqua regia in a microprocessor controlled digestion block at 90 °C for 2 h. After diluting the resultant solution, 28 elements were analyzed by inductively coupled plasma mass spectrometry (ICP-MS) using a Perkin-Elmer SCIEX ELAN 6,000; 6,100; or 9,000 ICP-MS. Digestion duplicates were analyzed every 15 samples. An in-house control was run every 33 samples, and blank and digested standards were run every 68 samples and instrument was recalibrated. Each batch of samples is bracketed by international reference materials, and duplicate and internal control standards are analyzed every 10 samples. Some silicates, oxides, and resistant materials such as zircon and monazite were not totally dissolved. For more precision on highly Mn-concentrated samples, a lithium metaborate/tetraborate fusion-ICP method was used. These samples were run with replicates, a method reagent blank, and certified reference material. Samples were fused in an induction furnace after mixing with lithium metaborate and lithium tetraborate. The molten melt was added to a 5% nitric acid solution with an internal standard, and mixed ∼30 min until completely dissolved. The samples were then run for manganese concentration on a combination simultaneous Thermo Jarrell-Ash ENVIRO II ICP or a sequential Varian Vista 735 ICP. The instrument is calibrated using seven certified reference materials. Data are available in Table S1.

Small samples for bulk XAS were chosen from Mn-rich intervals of both cores as well as several samples from strata with conspicuous but lower Mn concentrations (Table S1). A microrotary drill with a 1-mm bit was used to produce coarse powders of all visible textures, producing ∼100–200 mg of powder. These samples were loaded into small glass vials then transferred to an anaerobic chamber. In this chamber, a ceramic mortar and pestle was used to further grind this powder into a very fine, homogenous mixture. The powder was then spread evenly onto monolayers of Scotch tape to produce ∼6–14 layers, depending on Mn concentration. These monolayer tape samples were then stored in heat-sealed Mylar bags, except for one duplicate that was prepared and stored in air. The use of anaerobic glove box and vacuum bags were used to prevent any oxidation of reduced Mn in the samples. However, these extra steps were unnecessary as the XAS spectra of the same sample prepared both anaerobically and aerobically are identical (Fig. S2). This result is consistent with theory and measurements of abiotic Mn oxidation by O_2—a process that is strongly kinetically limited and proceeds very slowly in solution (14), and essentially does not occur in dry air.

Carbonate nodules and ankerite-dominated intervals were targeted for carbonate sampling using a microrotary drill with a 1-mm bit. These microsampled powders were stored in glass vials. Slabs and rounds were prepared from desired strata for analyses on the Scanning Electron Microscope (SEM), the Electron Microprobe (E-probe), on beam line (BL) 10–2 and 2–3 at Stanford Synchrotron Radiation Lightsource, and on the secondary ion mass spectrometry instrument (SIMS). Slabs were cut using a rock saw and rounds were made using a 1-inch drill press, targeting desired sections. Billets and rounds of ∼5 mm were made into thin sections by High Mesa Petrographics or Spectrum Petrographics, and carefully polished to obtain a microprobe quality surface. For use on the SEM and E-probe, returned thin sections were subsequently carbon coated with 7–15 nm of graphite using a Cressington Carbon Coater. Before analysis using the SIMS, thin sections were sputter coated with gold (30 nm) using a Cressington Sputter Coater. Ultrathin sections (∼10 μm) were made for XAS to minimize the amount of sample volume felt by the X-ray beam. The Mn concentration of the thin section glass is below the detection limit of our analyses.

Samples adjacent to sections prepared for in situ (SIMS) analyses were targeted for bulk sulfur measurements. These were removed from the core and cubed using a rock saw. They were then powdered using an SPEX 8510 Shatterbox to yield ∼2–5 g of sample. Extremely ^{34}S-enriched pyrite cements (as shown by in situ measurements, Fig. 4, Fig. S12, and Table S3) from fracture filling cements were also sampled using a microrotary drill for comparison with in situ measurements (yielding 1.2–2.1 mg, Table S3 labeled with ‘^’). In addition, an in-house pyrite standard used for in situ measurements was subsampled for analyses to assay standard homogeneity.

Bulk Powder X-Ray Absorption Spectroscopy

Beam line 4–1 at SSRL was used to analyze 16 samples for bulk manganese oxidation state and coordination environment. A Silicon 220 Φ = 90 crystal was used and X-ray absorption spectra (XAS) was collected on a Lytle detector for fluorescence and on an absorption detector for transmission spectra. A collimating mirror was used to help reduce harmonics in the beam, and a potassium permanganate [$KMn(VII)O_4$] standard was used for

calibration. Duplicates were run on all spectra collected for X-ray absorption near edge structure (XANES) scanning from 6,310 to 7,108 eV. Representative samples were targeted for X-ray absorption fine structure (XAFS) with ~4 repeats for higher Mn concentrations and ~10 repeats for lower Mn-bearing samples scanning from 6,310 to 7,223 eV.

XAS Mapping

Beam line 10–2 at SSRL was used to analyze 12 samples for coarse-resolution mapping. Polished thin sections (rounds or rectangular) were analyzed at three energies determined to distinguish redox states: 6,551; 6,562; and 6,572 eV. Maps were generated by collecting the X-ray fluorescence using a Fortex FII International Silicon drift detector on ~80 × 80 μm pixels (focused by capillary optics), which were rastered over the sections. Regions of interest were subsequently mapped in higher resolution on BL 2–3 at SSRL at ~10-μm resolution (with a 2-μm beam using Kirkpatrick Baez mirrors for focusing) on a Fortex FII International Silicon drift detector using four redox-distinctive energies determined from braunite and kutnohorite from the Kalahari Manganese Field (Figs. S3 and S4), using the maximal normalized fluorescence differences between these end members as targets for redox-distinguishing energies (Fig. S4). The braunite spectra were chosen as a representative end member as it captures the most oxidized (although still mixed valence) phase found in Mn-rich sedimentary rocks of similar diagenetic and metamorphic grade like nearby Kalahari Manganese Field. We chose kutnohorite as the reduced end member for our multiple energy maps as our bulk XAS spectra best matched the Kalahari kutnohorite (Fig. S3). The redox-distinguishing energies chosen for high-resolution maps were 6,542; 6,551; 6,560–62; and 6,572–73 eV, and sometimes 6,546; 6,548; 6,558; and 6,568 eV (Fig. S3). To rule out the presence of even small domains of Mn-oxide-bearing phases a multiple energy map at ~2-μm resolution was also generated for most of the samples (Fig. 2).

Multiple energy maps were analyzed using the MicroAnalysis Toolkit software (15). Maps of each energy were imported into one master file, thereby providing a set of distinctive absorptions at several energies for every map pixel (i.e., a mini-XANES spectrum, ref. 15). These pixels were then analyzed using a nonnegative linear–least squares fit of the data to the two end member spectra, an Mn(II)-bearing carbonate and an oxidized Mn(III)-bearing braunite from the Kalahari Manganese Field using the MicroAnalysis Toolkit fitting function. Normalized intensity of the absorption spectra of the two end members was determined for the energies measured, and then each pixel is fit to the composition of each standard. Subsequent confirmation of the fit is found by measuring XANES spectra at pixels identified as distinct by a principal component analysis of the multiple energies (15, 16). Fitted pixels were all set to the same scale, 0–1,500 counts for kutnohorite (Mn-bearing carbonate) and 0–4,000 counts for braunite. Fitted results agree within 5% (15) and all full XANES spectra collected at specific 2 × 2 μm points support the fitted-pixel redox maps.

To quantify Mn concentration, the highest energy map was used (6,572 or 6,573 eV). The manganese abundance was collected in counts, which were converted to units of micrograms per square centimeter using a map made at the same energy and under the same conditions (incident monochromator energy and detector distance) of an Mn foil, made from Mn deposited on a Mylar film at a concentration of 47.1 μg/cm^2. After removing edge effects of the standard map, a QuantFile of the standard was created to calibrate against the data files. Scales were then adjusted to the closest multiple of 50 for comparative purposes (scales range from 50 to 1,500 to best show small-scale variations of Mn).

SEM/E-Probe

A Zeiss 1550VP Field Emission Scanning Electron Microscope equipped with an Oxford INCA Energy 300 X-ray Energy Dispersive Spectrometer (EDS) system housed in the Geological and Planetary Sciences (GPS) Division Analytical Facility was used for all analyses. High-resolution images were taken in backscatter electron imaging mode to enhance compositional contrast. EDS measurements of X-ray fluorescence were made mainly on points (e.g., Fig. S3) but also as X-ray fluorescence maps (Fig. 3). Quantitative elemental analysis provides relative accuracy of better than 5%. These capabilities were used to identify detrital minerals such as pyrite and zircon, to examine pyrite nodules and fracture fills examined on the SIMS, and to investigate the textural complexity of samples from GTF01, GEC01 and from the Kalahari Manganese Field.

Other measurements were made on a JEOL JXA-8200 Advanced Electron Probe Microanalyzer (E-probe) equipped with five wavelength dispersive X-ray spectrometers (WDS), tungsten and LaB6 electron sources, and a detection limit of several hundred parts per million. It has an accuracy as good as 1–2% and the precision on pyrite is 0.2% (S) and 0.4% (Fe). The detection limit for manganese was 300 ppm, and all samples identified as pyrite phase (FeS_2) were below the Mn detection limit. A late-stage fracture with discontinuous pyrite mineralization (characterized by heavy $\delta^{34}S$ values) (Fig. S12) was examined on the E-probe and the concentration of manganese was measured from spots throughout the mineralized fracture. The Mn concentration was below detection limit for 40 measurements and below 0.1% of the total concentration for the remaining measurements, discounting three outliers (Fig. S5). These outliers were measurements made on nonpyrite but instead capturing (partially or totally) some of the Mn-bearing matrix. Even including the outliers, the total Mn percentage is less than 0.5% in all points measured, highlighting the lack of Mn delivery from metasomatic fluids.

Carbonate C and O Isotopic Analysis

Carbonate samples were measured for their carbon isotopic distribution at the University of Michigan Stable Isotope Laboratory. Samples are heated to 200 °C for one hour, removing any volatile contaminants and water. Samples are then reacted at 77 ± 1 °C with anhydrous phosphoric acid for 22 min in individual borosilicate reaction vessels in a Finnigan MAT Kiel IV preparation device. This is directly coupled to the inlet of a Finnigan MAT 253 triple collector isotope ratio mass spectrometer, which measures isotopic measurements calibrated against National Bureau of Standards (NBS) 18 and NBS 19. Data are reported in delta notation (percent) relative to VPDB and measured precision is better than 0.1‰ assessed by multiple analyses of a variety of carbonate standards. The data are available in Table S2. Estimates for the carbon isotopic composition of dissolved inorganic carbonate (DIC) during this time period were derived from Bekker (17) and Fischer et al. (18) (Fig. 3).

Bulk S Isotope Analysis by SF_6 Gas Source Mass Spectrometry

At the MIT Stable Isotope Laboratory, pyrite sulfur was extracted from powdered rock samples by chromium chloride reduction following a method modified from (17). A 1-M $CrCl_3$ solution was reduced using zinc metal (4 g zinc/40 mL of $CrCl_2$). Sample powders (1.5 to 5 g) were added to a round bottom flask connected to a condenser with a sidearm to allow N_2 to flow through. The condenser was connected to a water trap filled with 60–70 mL of DI H_2O for condensed phases and a trap containing ~50 mL of zinc acetate. Approximately 30 mL of chromium chloride solution was added to the sample powders after flushing and then heated to boiling for 2–3 h to drive off H_2S and ulti-

mately precipitate ZnS. Once the reaction has completed, silver nitrate is added (5 mL) to react with the zinc sulfide and form precipitated silver sulfide (Ag_2S). The precipitates are washed with NH_4OH (to remove any silver hydride) and ultrapure DI water and dried. The silver sulfide was then reacted with F_2 at 300 °C. Reacted SF_6 is transferred via liquid nitrogen cold traps, removing any extraneous F_2, and purified by means of a gas chromatograph. The SF_6 is then fed into a Thermo 253 dual-inlet mass spectrometer, where the isotopes ratios sulfur isotopes (^{32}S ^{33}S ^{34}S ^{36}S) were measured against in-house standards. This method offers a precision of 0.26, 0.014, and 0.19‰ (2σ) for $\delta^{34}S$, $\Delta^{33}S$, and $\Delta^{36}S$ values based on multiple measurements of reference materials [International Atomic Energy Agency (IAEA) standards; IAEA S-1: $\delta^{34}S$ −1.34 ± 0.13, $\Delta^{33}S$ 0.10 ± 0.007, and $\Delta^{36}S$ −0.57 ± 0.10; IAEA S-2: $\delta^{34}S$ 21.18 ± 0.13, $\Delta^{33}S$ 0.043 ± 0.005; and $\Delta^{36}S$ −0.16 ± 0.05; IAEA S-3: $\delta^{34}S$ −33.54 ± 0.13, $\Delta^{33}S$ 0.091 ± 0.020, and $\Delta^{36}S$ −0.58 ± 0.11]. The data are reported in delta notation (per mil) with respect to VCDT, and are reported in Table S3.

In Situ S Isotope Analysis by Secondary Ion Mass Spectrometry

We used a Cameca 7f-GEO, a pseudo multicollector SIMS instrument with three separate collectors that measure different ions in rapid succession by dynamic peak hopping, housed within the Center for Microanalysis at the California Institute of Technology. The instrument was operated at a primary beam current of ∼3 nA with a spot size of ∼25 μm. We measured ^{32}S, ^{33}S, and ^{34}S with a mass resolving power of ∼4,000 to separate ^{33}S from ^{32}SH, and typically achieved $\sim10^9$ counts s^{-1} of ^{32}S, and $\sim10^8$ and $\sim10^7$ counts s^{-1} for ^{34}S and ^{33}S, respectively. Sample unknowns were bracketed by measurements of an in-house pyrite standard ($\delta^{34}S$ 1.024‰, $\delta^{33}S$ 0.608‰), comounted in epoxy close to the regions of the sample of interest and polished to obtain the same flat analytical surface. Data were corrected for Faraday cup yield differences (^{32}S was collected on Faraday cup 1 and ^{33}S and ^{34}S are collected on Faraday cup 2) and instrumental mass fractionation of isotopes. External precision (defined as the SD of multiple adjacent measurements of standards) is typically better than $\delta^{34}S$ = 0.4‰, $\delta^{33}S$ = 0.3‰, $\Delta^{33}S$ = 0.15‰. (For measurements on detrital pyrite grains, precision is similar for $\Delta^{33}S$ but is up to 1.3‰ for $\delta^{34}S$ as standards were not on same mount adjacent to pyrite). The data are reported in delta notation in per million with respect to VCDT, and is available in Table S3.

Kinetics of Manganese Oxidation by O_2

Mn(II) oxidation by the low levels of molecular oxygen allowable by our independent redox proxies does not explain the enrichments observed in Koegas strata. Although thermodynamics dictate molecular oxygen will oxidize Mn(II) at far less than 10^{-10} atm, oxidation reactions by O_2 are strongly kinetically limited (14, 19). Even at modern oxygen levels, abiological manganese oxidation is exceedingly slow—kinetic limitations result in an Mn (II) half life of 30 d for oxide-stimulated oxidation and 400 d for a homogenous solution with $Mn^{2+}{}_{(aq)}$ and O_2 (under a 0.21 atm pO_2 atmosphere) (14). Considering molecular oxygen produced in the surface ocean will reside for an average of ∼17 d before escaping to the atmosphere (20), abiological mechanisms are not rapid enough to produce the volume of manganese we observe.

Biological manganese oxidation (using O_2) proceeds more rapidly and is thought to be the main mechanism for Mn oxidation in modern environments—under today's atmosphere, Mn(II) has a half life of 10 h (14). This process is most efficient at enzyme saturation, at a range of 0.87–11 μM of dissolved O_2 (the Michaelis–Menton constant K_M, ref. 21). Oxygen levels during Koegas deposition were likely around 10^{-13} atm (22) [the predicted O_2 levels for the atmosphere before the rise of cyanobacteria (23), dissolved O_2 would be $1.26*10^{-7}$ nM], but constrained by multiple sulfur isotope data to be at most lower than $10^{-5.7}$ atm (dissolved O_2 would be 2.6 nM) (22). We used these two estimates of atmospheric oxygen to determine the amount of manganese that could be oxidized at these low O_2 levels. Using the lowest reported value for measured biological Michaelis–Menton constants (K_M = 0.87 μM, ref. 21), the highest values for maximum Mn(II)-oxidation rates at infinite O_2 (V_{Max} = 50 nM/h, ref. 21), we estimated a maximum rate of Mn-oxide production using saturation kinetics calculations (21):

$$\text{Oxidation rate of Mn(II)} = (s * V_{Max})/(K_M + s).$$

At the likely precyanobacteria levels of 10^{-13} atm of O_2, the Mn oxidation rate is $7.24 * 10^{-9}$ nM/h, or $3.48 * 10^{-9}$ $g{\cdot}L^{-1}{\cdot}ky^{-1}$. At the highest permitted O_2 concentrations of $10^{-5.7}$ atm, the Mn oxidation rate is 0.151 nM/h, or 0.073 $g{\cdot}L^{-1}{\cdot}ky^{-1}$.

These rates can be considered in the context of the processes delivering sediment to this basin. Koegas Subgroup lithologies describe a mixed clastic–chemical sedimentary basin with intercalated sequences of wave-modified deltaic siliciclastic sediments and iron formation (4, 5, 24). Iron formations here are often cross-bedded and granular, implying high wave action, and contain admixtures of sand, silt, and detrital aluminosilicate minerals further indicating competing terrigenous detrital influxes and chemical sedimentation (5) (Fig. 3 *A* and *B*). We estimate a seawater depth of ∼10 m for the GTF01 core, where sandstone intervals better constrain the water depth. Sedimentation rates can be approximated using measured rates for similar sedimentary basins and processes, with the assumption of uniform physical processes of sediment transport. Sadler (1981) constructed a vast compilation of ∼25,000 rate measurements and determined that sedimentation rates vary depending on integration time span (25). With delta lobe switching occurring at ∼3-y to 1,500-y intervals (26), terrigenous shelf delta and shelf seas sedimentation rates vary from ∼300 to ∼2 m/ky (27). We conservatively use 1 m/ky as the lowest background sediment accumulation rate during Mn deposition. Alternatively, Barley et al. (1997) estimated sedimentation rates for the deposition of banded iron formations in the Hamersley Basin, a shallow marine platform of slightly older age in Western Australia, suggesting rates between 0.1 and 1 m/ky using U-Pb zircon dating (interpolated from rates in meters per my) (28). These rates have been used in other geobiological calculations for iron formation deposition (29), and although it is an imperfect process and geodynamic basinal analog for the deposits examined here [as the Hamersley Basin was a siliciclastic-starved marine platform without significant river detrital flux (30)], we also use these rates for comparison.

We converted our Mn-oxidation rate calculations for different oxygen concentration scenarios into the mass of Mn deposited per thousand years and divided by the sediments accumulated in that time. A 10-m water column overlying a 1 × 1 cm square of sea floor is equal to 1 L of water in which Mn could be oxidized by O_2. For the same area, continental shelf sedimentation rates would predict 100 cm^3 deposited in 1,000 y (25), and the starved marine platform rates would estimate 10–100 cm^3/ky (28). Mass of the sedimentary column can be determined using an average density of iron formations, 3.45 g cm^{-3}, from (31). Applying these calculations to the Mn rates determined above, at 10^{-13} atm, the percent Mn in the sediments is insignificant: the Mn oxides produced by O_2 are $1.01*10^{-9}$% of the sediments using shelf seas and delta sedimentation rates and $1.01*10^{-8}$% of the sediments using the lowest starved marine platform sedimentation rates. At the highest O_2 levels allowed by our proxies, Mn oxides are 0.02% of the sediments using the higher shelf rates and 0.2% of the sediments using the lower starved platform rates. Thus, the nM-dissolved oxygen concentrations maximally allowed by multiple sulfur isotopes are not sufficient for producing the Mn enrichments

observed throughout our cores in both shallow and deep-water paleoenvironments. These calculations do not account for any Mn loss back to the water column from pore fluids during reduction. Including a fraction of recycled Mn in these kinetic calculations would just further highlight the discordance between the required rates and the exceedingly low O_2 concentrations indicated by the detrital pyrite and anomalous sulfur isotope fractionations. Simply put, Mn oxidation by O_2—either abiologically or biologically—is too slow to account for our observed enrichments.

There are few other mechanisms to potentially oxidize manganese. Biological Mn oxidation using nitrate is thermodynamically feasible but does not appear to occur in nature (21, 32). Hydrogen peroxide can oxidize manganese, but production of a large volume of H_2O_2 would require a local source ice (33) and these deposits accumulated in a tropical paleolatitude (34). Photooxidation of manganese occurs at insignificant levels when dissolved iron is present (35). This points to photobiology as the process of Mn oxidation and concentration in the sediments.

1. Pickard A (2003) SHRIMP U–Pb zircon ages for the Palaeoproterozoic Kuruman Iron Formation, Northern Cape Province, South Africa: Evidence for simultaneous BIF deposition on Kaapvaal and Pilbara Cratons. *Precambrian Res* 125:275–315.
2. Trendall AF, et al. (1990) Precise zircon U–Pb chronological comparison of the volcano-sedimentary sequences of the Kaapvaal and Pilbara Cratons between about 3.1 and 2.4 Ga. *Proceedings of the Third International Archaean Symposium*, eds Glover JE, Ho SE (Geological Society of Australia, Perth, Australia), pp 81–83.
3. Nelson DR, Trendall AF, Altermann W (1999) Chronological correlations between the Pilbara and Kaapvaal cratons. *Precambrian Res* 97(3–4):165–189.
4. Beukes NJ (1983) Palaeoenvironmental setting of iron-formations in the depositional basin of the transvaal supergroup, South Africa. *Developments in Precambrian Geology*, eds Trendall AF, Morris RC (Elsevier, Amsterdam), pp 131–198.
5. Schröder S, Bedorf D, Beukes NJ, Gutzmer J (2011) From BIF to red beds: Sedimentology and sequence stratigraphy of the Paleoproterozoic Koegas Subgroup (South Africa). *Sediment Geol* 236(1–2):25–44. Available at www.sciencedirect.com/science/journal/00370738.
6. Kirschvink JL, et al. (2000) Paleoproterozoic snowball earth: Extreme climatic and geochemical global change and its biological consequences. *Proc Natl Acad Sci USA* 97(4):1400–1405.
7. Walraven F, Armstrong R, Kruger F (1990) A chronostratigraphic framework for the north-central Kaapvaal craton, the Bushveld Complex and the Vredefort structure. *Tectonophysics* 171(1–4):23–48.
8. Armstrong RA (1987) Geochronological studies on Archean and Proterozoic Formations of the Namaqua Front and possible correlates on the Kaapvaal Craton. PhD thesis (University of Witwatersrand).
9. Cornell DH, Schütte SS, Eglington BL (1996) The Ongeluk basaltic andesite formation in Griqualand West, South Africa: Submarine alteration in a 2222 Ma Proterozoic sea. *Precambrian Res* 79(1–2):101–123.
10. Gutzmer J, Beukes N (1998) *High-Grade Manganese Ores in the Kalahari Manganese Field: Characterisation and Dating of Ore Forming Events* (Rand Afrikaans University, Johannesburg).
11. Beukes NJ, Gutzmer J (2008) Origin and paleoenvironmental significance of major iron formations at the Archean-Paleoproterozoic boundary. *Banded Iron Formation-Related High-Grade Ore*, eds Hagemann S, Rosiere C, Gutzmer J, Beukes N (Society of Economic Geologists, Littleton, CO), pp 5–47.
12. Polteau S, Moore JM, Tsikos H (2006) The geology and geochemistry of the Palaeoproterozoic Makganyene diamictite. *Precambrian Res* 148(3–4):257–274.
13. Hoffman PF (2013) The Great Oxidation Event and a Siderian Snowball Earth: MIF based correlation of Paleoproterozoic glaciations. *Chem Geol*, 10.1016/j.chemgeo.2013.04.018.
14. Morgan JJ (2005) Kinetics of reaction between O2 and Mn(II) species in aqueous solutions. *Geochim Cosmochim Acta* 69(1):35–48.
15. Webb SM (2006) SMAK: Sam's Microprobe Analysis Kit (Stanford Synchrotron Radiation Laboratory, Melo Park, CA), v.0.25.
16. Mayhew LE, Webb SM, Templeton AS (2011) Microscale imaging and identification of Fe speciation and distribution during fluid-mineral reactions under highly reducing conditions. *Environ Sci Technol* 45(10):4468–4474.
17. Bekker A, et al. (2001) Chemostratigraphy of the Paleoproterozoic Duitschland Formation, South Africa: Implications for coupled climate change and carbon cycling. *Am J Sci* 301(3):261–285.
18. Fischer WW, et al. (2009) Isotopic constraints on the Late Archean carbon cycle from the Transvaal Supergroup along the western margin of the Kaapvaal Craton, South Africa. *Precambrian Res* 169(1–4):15–27.
19. Luther GW III (2010) The role of one- and two-electron transfer reactions in forming thermodynamically unstable intermediates as barriers in multi-electron redox reactions. *Aquat Geochem* 16(3):395–420.
20. Broecker WS, Peng T-H (1982) *Tracers in the Sea* (Columbia University, Palisades, NY).
21. Clement BG, Luther GW III, Tebo BM (2009) Rapid, oxygen-dependent microbial Mn(II) oxidation kinetics at sub-micromolar oxygen concentrations in the Black Sea suboxic zone. *Geochim Cosmochim Acta* 73(7):1878–1889.
22. Pavlov AA, Kasting JF (2002) Mass-independent fractionation of sulfur isotopes in Archean sediments: strong evidence for an anoxic Archean atmosphere. *Astrobiology* 2(1):27–41.
23. Kasting JF (1993) Earth's early atmosphere. *Science* 259(5097):920–926.
24. Beukes NJ (1978) Die karbonaatgesteentes en ysterformasies van die Ghaap-Groep van die Transvaal-Supergroep in Noord-Kaapland. PhD thesis (Rand Afrikaans University).
25. Sadler P (1981) Sediment accumulation rates and the completeness of stratigraphic sections. *J Geol* 89(5):569–584.
26. Jerolmack DJ, Mohrig D (2007) Conditions for branching in depositional rivers. *Geology* 35(5):463–466.
27. Sadler PM, Hass HC (1999) The influence of hiatuses on sediment accumulation rates. *On the Determination of Sediment Accumulation Rates*, ed Bruns P (Trans Tech Publications, Durnten-Zurich, Switzerland), pp 15–40.
28. Barley ME, Pickard AL, Sylvester PJ (1997) Emplacement of a large igneous province as a possible cause of banded iron formation 2.45 billion years ago. *Nature* 385:55–58.
29. Konhauser KO, et al. (2002) Could bacteria have formed the Precambrian banded iron formations? *Geology* 30(12):1079–1082.
30. Blake TS, Barley ME (1992) Tectonic evolution of the Late Archaean to Early Proterozoic Mount Bruce Megasequence Set, western Australia. *Tectonics* 11(6):1415–1425.
31. Ewers WE, Morris RC (1981) Studies of the Dales Gorge Member of the Brockman Iron Formation, Western Australia. *Econ Geol* 76(7):1929–1953.
32. Schippers A, Neretin LN, Lavik G, Leipe T, Pollehne F (2005) Manganese(II) oxidation driven by lateral oxygen intrusions in the western Black Sea. *Geochim Cosmochim Acta* 69(9):2241–2252.
33. Liang M-C, Hartman H, Kopp RE, Kirschvink JL, Yung YL (2006) Production of hydrogen peroxide in the atmosphere of a Snowball Earth and the origin of oxygenic photosynthesis. *Proc Natl Acad Sci USA* 103(50):18896–18899.
34. Evans DA, Beukes NJ, Kirschvink JL (1997) Low-latitude glaciation in the Palaeoproterozoic era. Nature 386(6622):262–266.
35. Anbar AD, Holland HD (1992) The photochemistry of manganese and the origin of Banded Iron Formations. *Geochim Cosmochim Acta* 56(7):2595–2603.

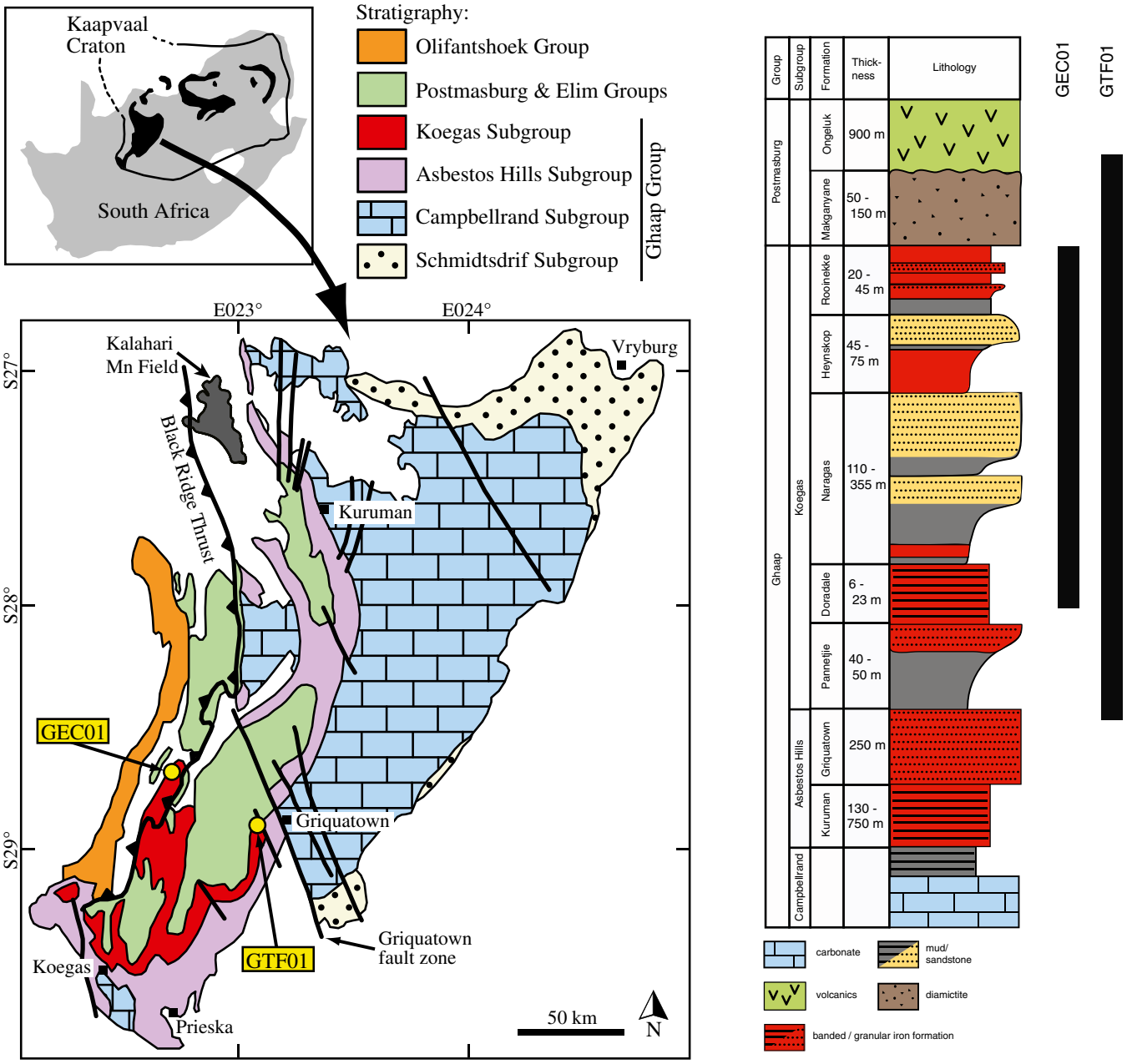

Fig. S1. Geologic map of Archean- and Paleoproterozoic-age strata exposed in Griqualand West subbasin of the Transvaal Supergroup, South Africa, modified from ref. 5 with permission from Elsevier. Note the location of drill cores GTF01 and GEC01. (*Right*) A generalized stratigraphic column with lithologic information showing the stratigraphic breadth of the two drill cores.

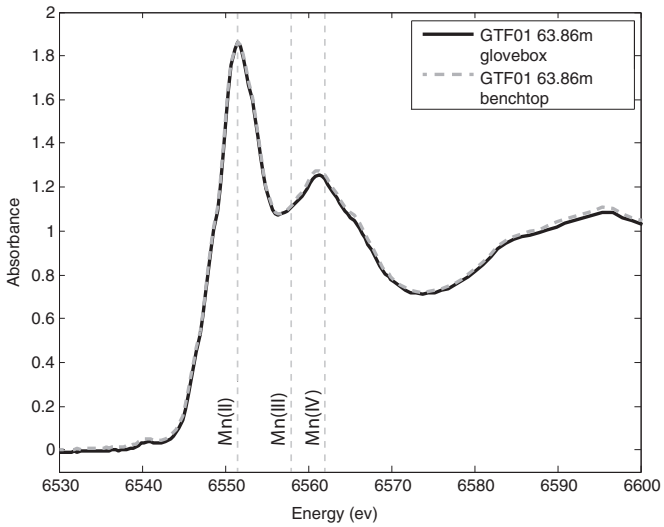

Fig. S2. Bulk X-ray absorption spectra of one sample (GTF01 at 63.86 m) prepared both in an anaerobic glovebox and on an aerobic bench top and measured on beam line 4–3 at SSRL. Maximal absorptions for Mn(II), Mn(III), and Mn(IV) are shown for reference. Spectra are indistinguishable, indicating lack of Mn oxidation from exposure to oxygen over a timescale of ~1 wk.

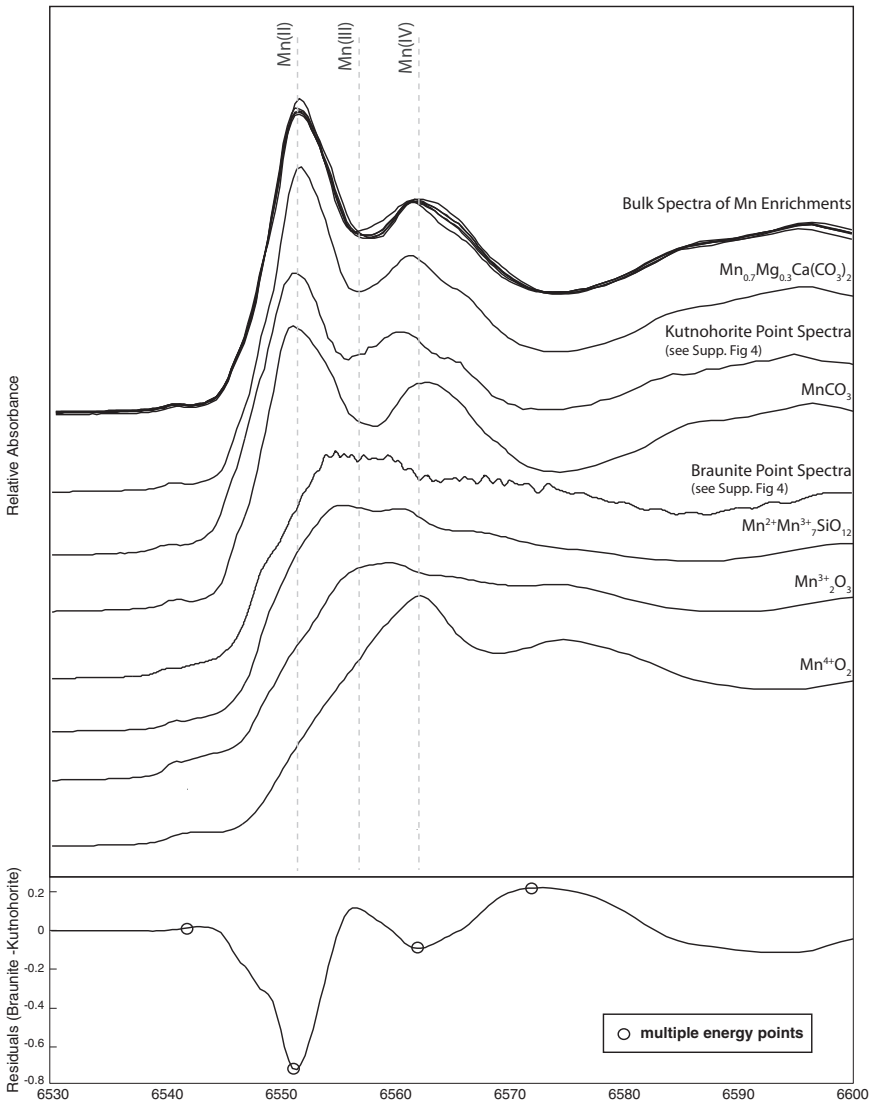

Fig. S3. (*Upper*) X-ray absorption spectra of known Mn-bearing minerals: well-characterized kutnohorite and braunite from the Kalahari Manganese Field, rhodochrosite, and Mn(III) and Mn(IV) oxides. Mn(II) in carbonate phases show XANES spectra easily distinguishable from mixed valence manganese (II and III) in braunite [$Mn(II)Mn(III)_4(SiO_4)O_8$] and other species with oxidized Mn. Compare these to bulk spectra of all Koegas Mn enrichments from GEC01 and GTF01 ($n = 16$) and point spectra from carbonate concretions and oxide matrix of the Kalahari. Bulk Koegas spectra and carbonate concretions from the Kalahari best-match kutnohorite spectra. Also shown by vertical lines are maximal absorption energies of Mn(II), Mn(III), and Mn(IV). *Lower* plots residuals when subtracting Kalahari kutnohorite from braunite. Black circles indicate the X-ray energies commonly used to distinguish Mn redox states.

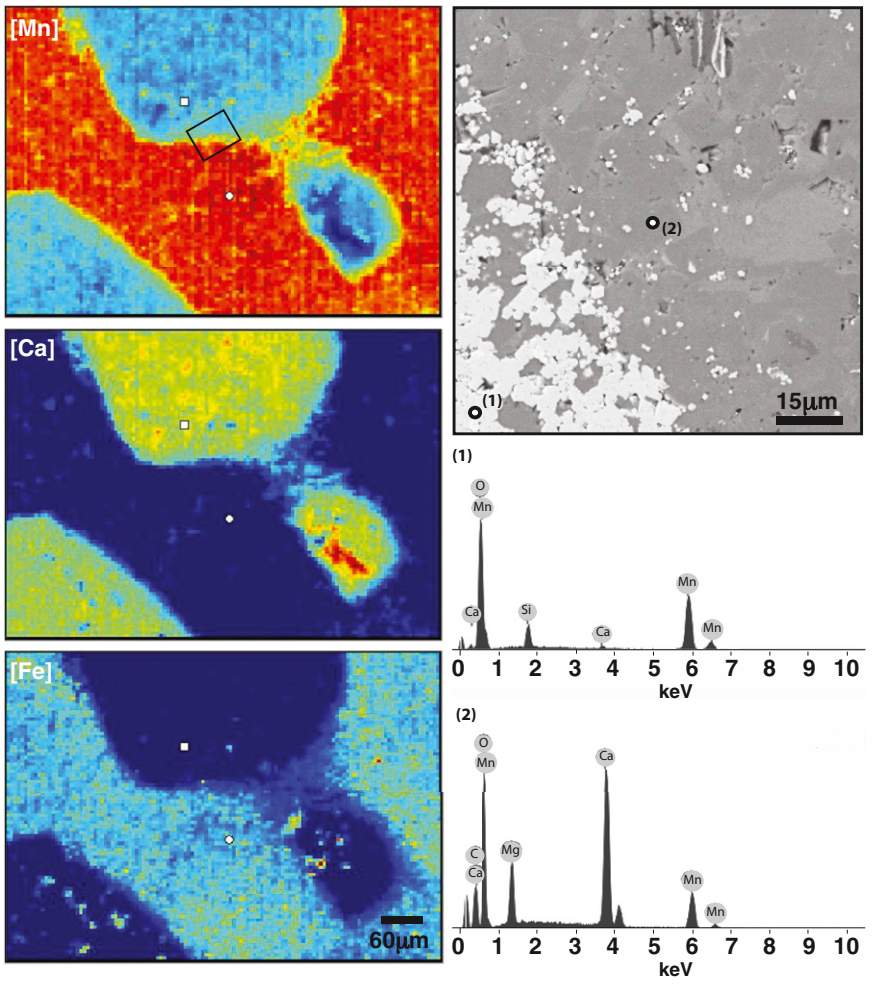

Fig. S4. (*Left*) X-ray fluorescence (XRF) maps of Mn, Ca, and Fe abundance on a sample from the Kalahari Manganese Field. Small white squares mark positions of spots where kutnohorite and braunite spectra were measured to obtain end member spectra (Fig. S3) for multiple energy redox maps presented in Fig. 2. (*Right*) SEM backscatter image of the domain highlighted in the black box on the left. EDS spectra on the first and second marked circles highlight the composition of braunite and kutnohorite, respectively.

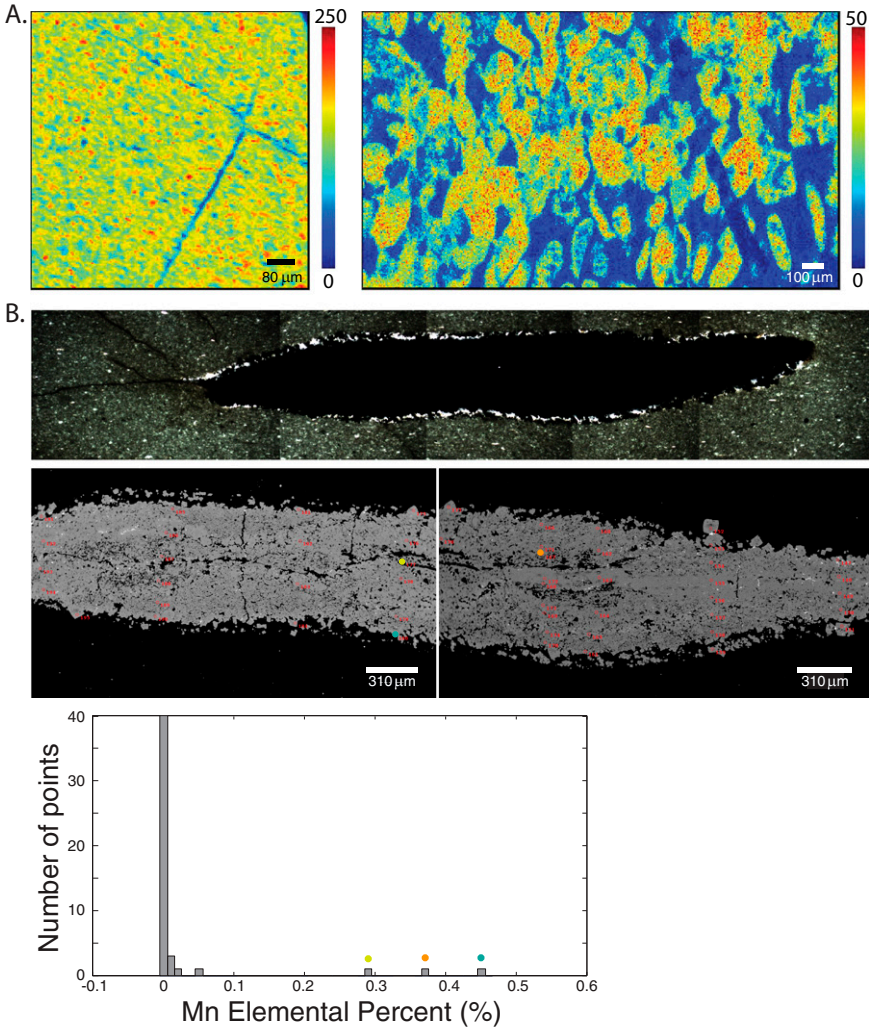

Fig. S5. (*A*) Manganese concentration in micrograms per square centimeter measured by X-ray fluorescence at SSRL. Mn concentrations are much lower in mineralized late cracks and fractures, indicating Mn enrichments did not originate from late fluids. (*B*) Transmitted light photomicrograph (*Upper*) and backscatter SEM image (*Lower*) of GEC01 169.83 m showing discontinuous pyrite mineralization along a fracture. *Bottom* is a histogram of Mn concentration from electron probe measurements. Outliers with higher Mn abundance are shown as yellow, orange, and blue dots. Note the positions of these anomalous spot analyses occur in regions that incorporate more matrix and are not solely pyrite.

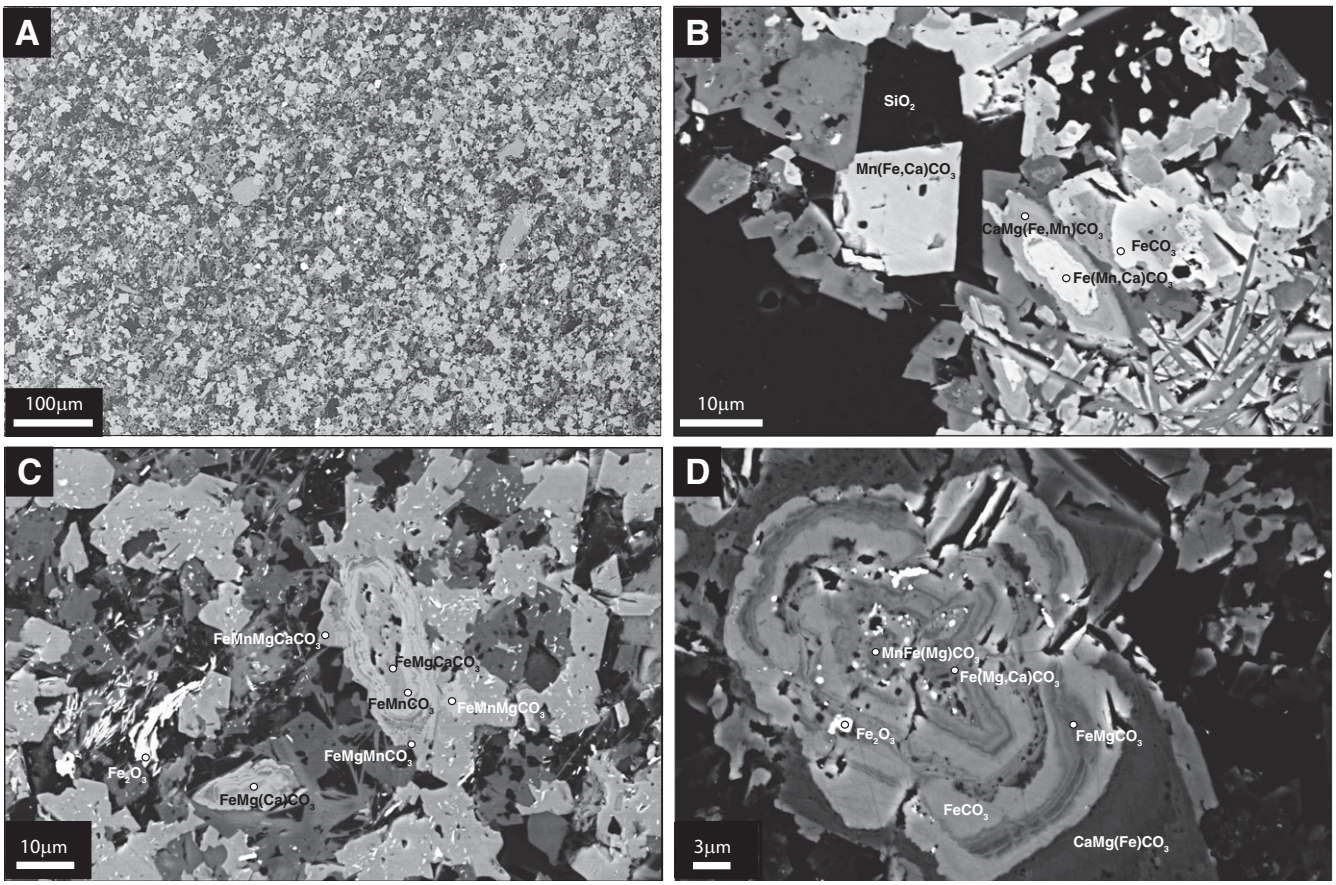

Fig. S6. SEM backscatter images of samples enriched in Mn reveal very fine-grained mixtures of oxide, silicate, and carbonate phases with diagenetic textures. (*A* and *C*) from GTF 111.15 m; (*B* and *D*) from GTF 54.10 m.

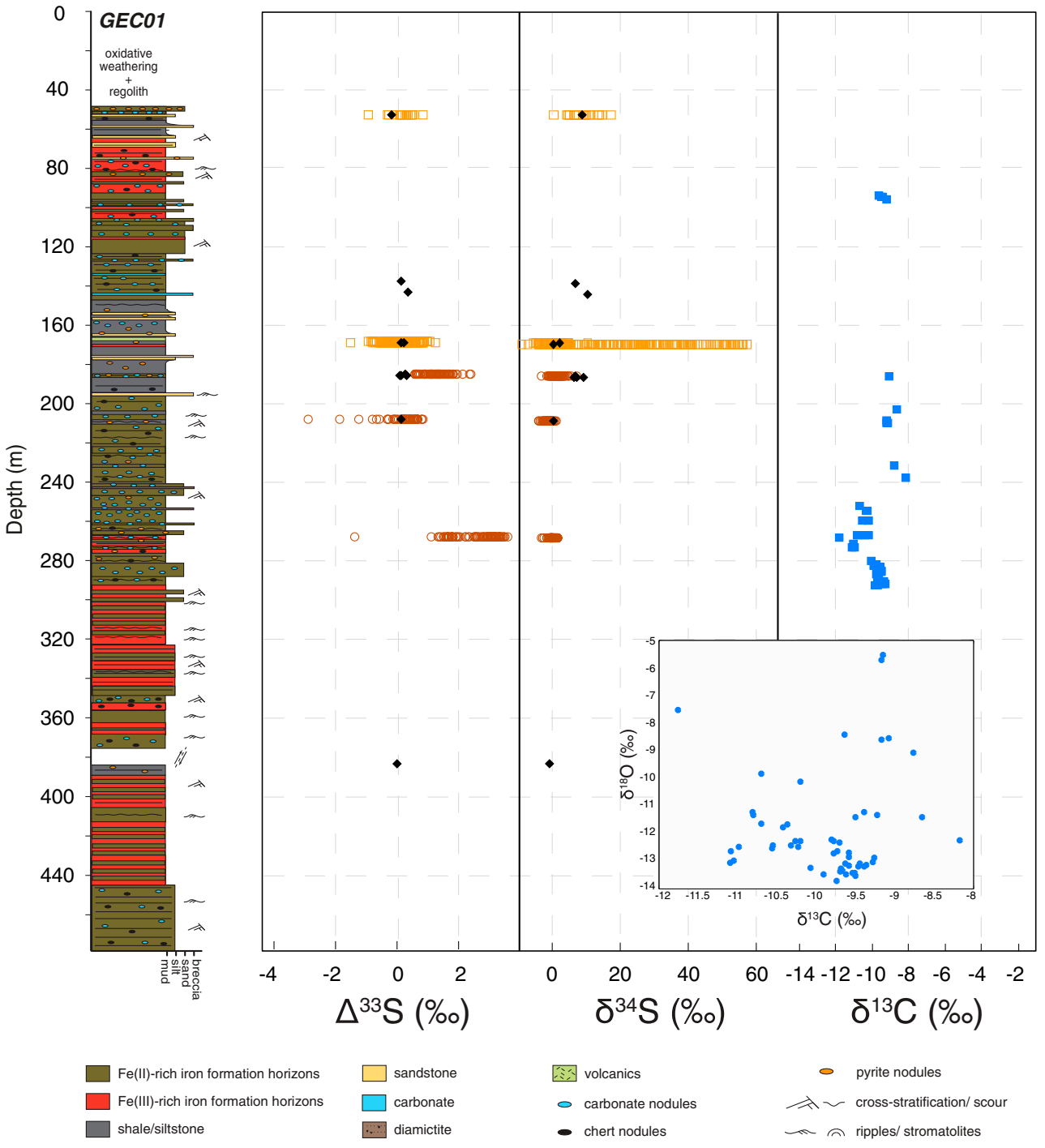

Fig. S7. GEC01 core with sulfur isotopic data ($\Delta^{33}S$ and $\delta^{34}S$) and carbon isotopic data ($\delta^{13}C$; blue) plotted with depth. Maroon circles mark in situ primary pyrite, orange squares signify in situ measurements of late pyrite, and black diamonds designate bulk SF_6 measurements.

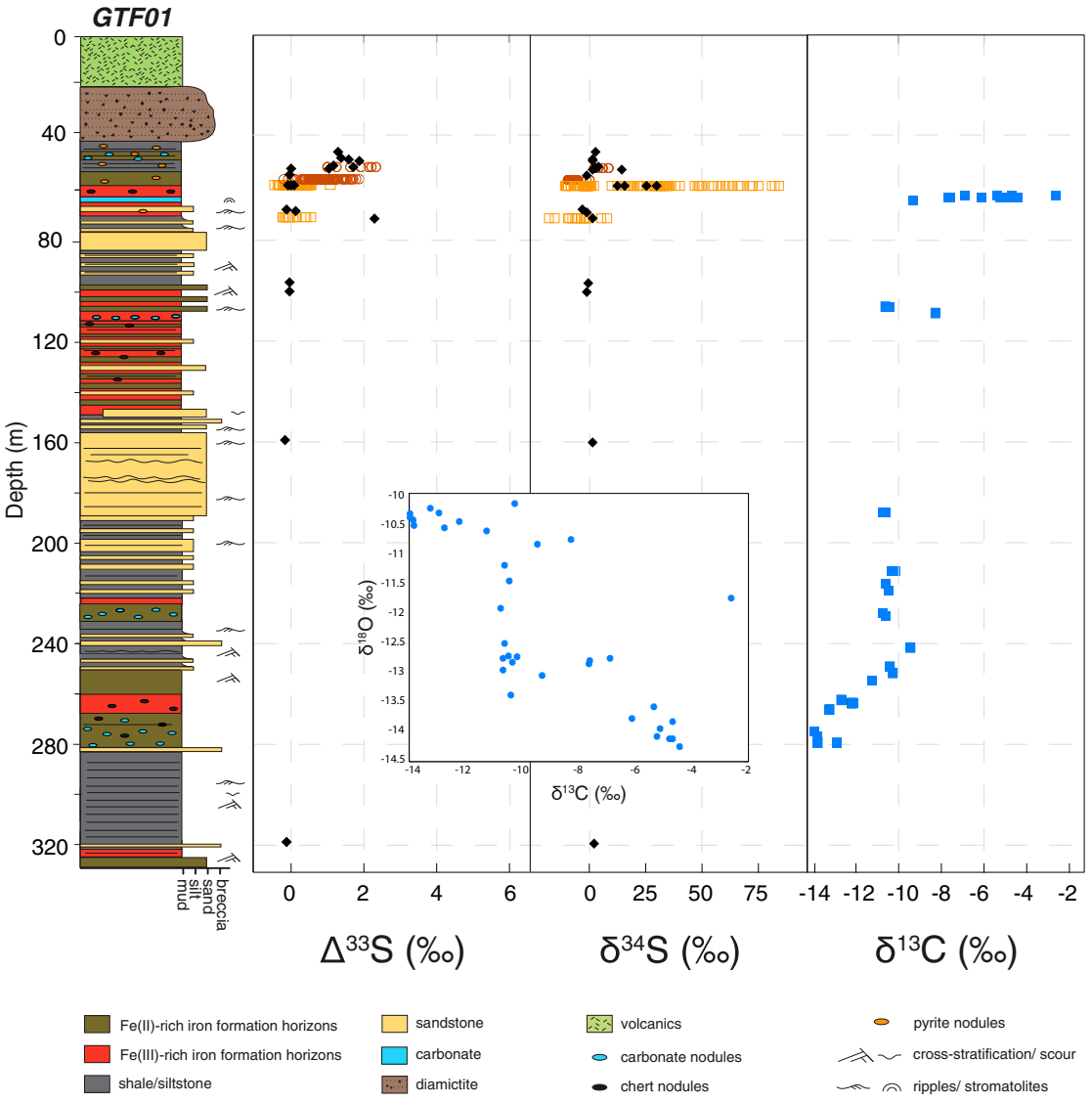

Fig. S8. GTF01 core with sulfur isotopic data ($\Delta^{33}S$ and $\delta^{34}S$) and carbon isotopic data ($\delta^{13}C$; blue) plotted with depth. Maroon circles mark in situ primary pyrite, orange squares signify in situ measurements of late pyrite, and black diamonds designate bulk SF_6 measurements.

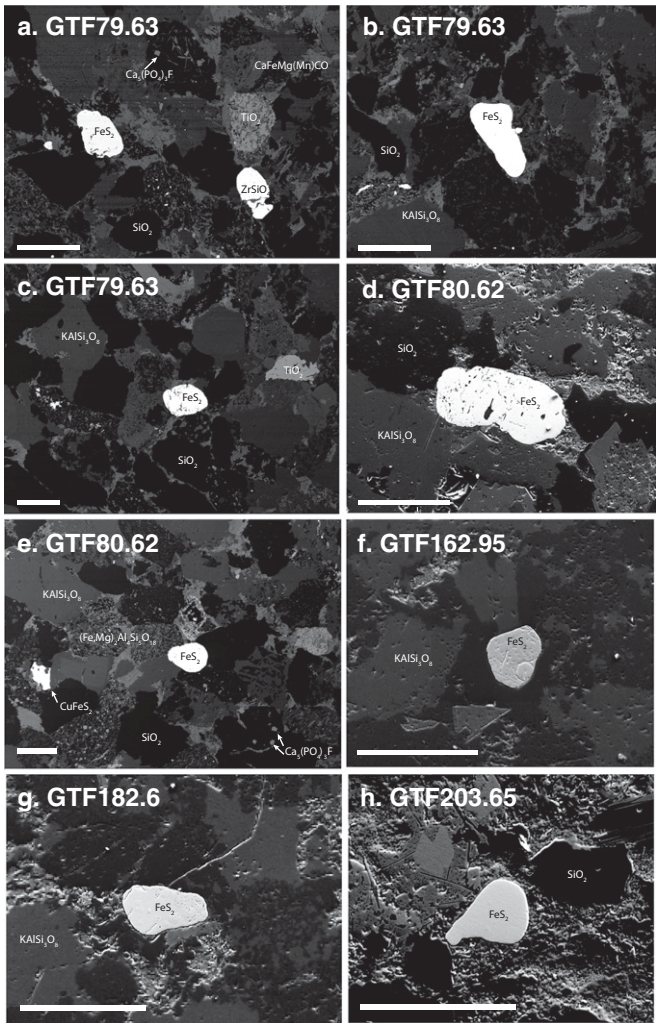

Fig. S9. SEM backscatter images of detrital pyrite grains from sandstone subunits in GTF01. Note the relative sizes, correlation with other heavy minerals, and rounding of detrital pyrites in examples *A*–*H* from throughout the core. Scale bars are 100 μm.

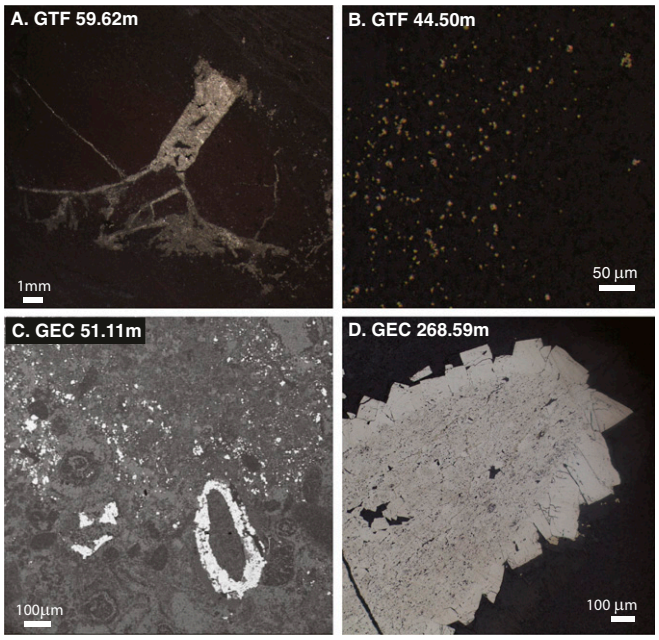

Fig. S10. Photomicrographs from light and scanning electron microscopy highlighting examples of late pyrite textures. (*A*) GTF01 at 59.62 m a fractured chert nodule hosting pyrite, (*B*) GTF01 at 44.50 m shows finely disseminated but sharply euhedral grains, (*C*) GEC01 at 51.11 m shows replacement of iron silicate and iron carbonate ooilitic grains by pyrite, and (*D*) GEC01 at 268.59 m shows a nodule with a coarse euhedral rim.

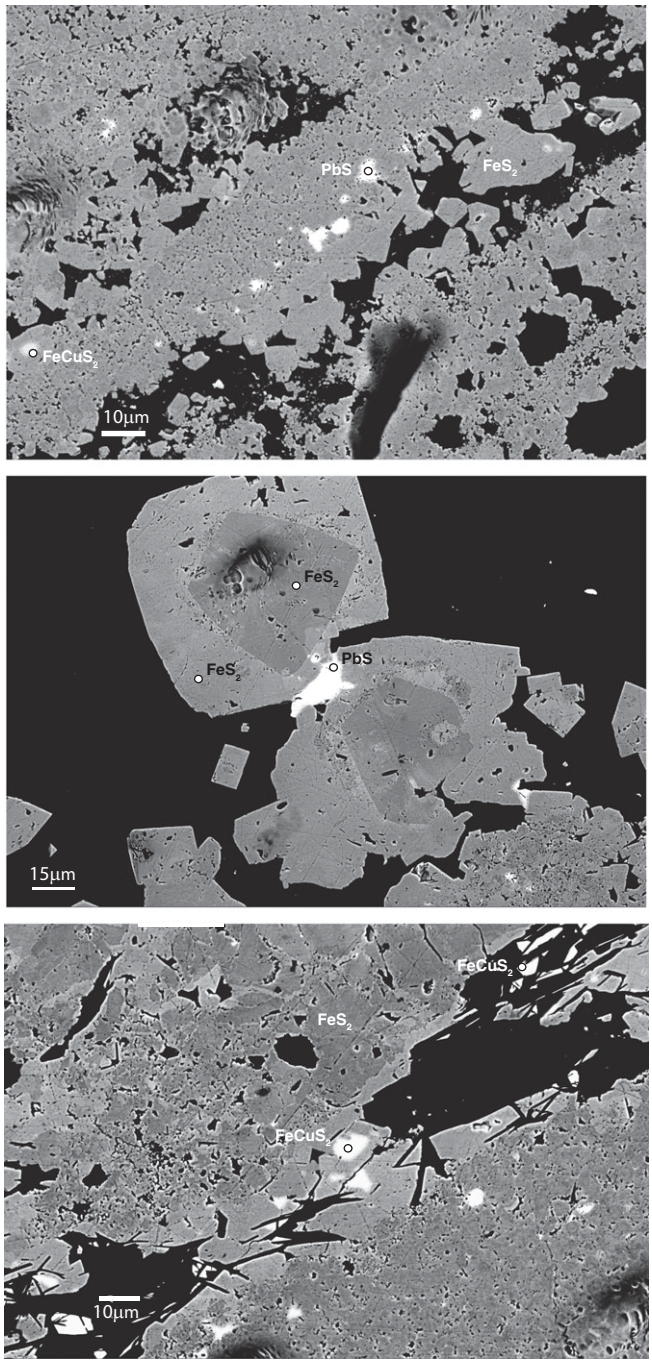

Fig. S11. Backscatter electron photomicrographs of pyrites with late diagenetic textures and domains of chalcopyrite ($FeCuS_2$) and galena (PbS), highlighting several episodes of sulfide mineralization in these strata.

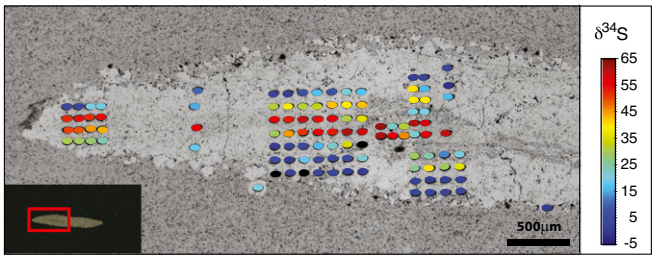

Fig. S12. Example of in situ sulfur isotopic measurements from GEC01 at 169.83 m on top of a backscatter electron image. This pyrite "nodule" is composed of aggregates of euhedral domains that grew from a through-going fracture. The extremely enriched isotopic values indicate large closed-system fractionation and perhaps thermochemical sulfate reduction from late hydrothermal fluids during late diagenesis and burial metamorphism. Color bar corresponds to $\delta^{34}S$ isotopic values (in per million VCDT), ranging from −5% to 65%.

Other Supporting Information Files

Table S1 (DOCX)
Table S2 (DOCX)
Table S3 (DOCX)